Journal of Food Composition and Analysis 159 (2026) 109633

Contents lists available at ScienceDirect

Journal of Food Composition and Analysis

journal homepage: www.elsevier.com/locate/jfca

Wheat kernel morphology as a potential confounding factor in spectroscopy-based analysis of intact kernels

Simon Ian Futerman [a,*], Eyal Ben Dor [a], Nir Sade [b], Israel Oren [b], Antonios Morellos [c], Abdul Mounem Mouazen [c]

[a] Remote Sensing Laboratory, Porter School of the Environment and Earth Sciences, Faculty of Exact Sciences, Tel Aviv University, Tel Aviv 699780, Israel
[b] School of Plant Sciences and Food Security, The Institute for Cereal Crops Improvement, Tel Aviv University, Tel Aviv 69978, Israel
[c] Precision Score and Crop Engineering Laboratory, Department of Environment, Faculty of Bioscience Engineering, Ghent University, Coupure Links 653, Blok B, 1st Floor, Gent 9000, Belgium

ARTICLE INFO

Keywords:
Machine learning
RGB image processing
Wheat kernel morphology
Wheat kernel spectral reflectance

ABSTRACT

Non-destructive evaluation of whole-grain quality is important for agricultural, nutritional, and industrial applications. This study investigated relationships between wheat kernel morphology, derived from a calibrated smartphone RGB imaging workflow, and bulk-sample spectral reflectance across the visible, near-infrared, and shortwave infrared regions (400–2450 nm). The RGB workflow used physical reference objects for spatial calibration, followed by independent validation with separate reference balls, which showed absolute measurement errors of < 0.1–0.2 mm. Ridge regression models were used to assess relationships between spectral information and morphological and mass-related traits. Thousand-kernel weight (test $R^2 = 0.59$), aspect ratio ($R^2 = 0.57$), and circularity ($R^2 = 0.46$) showed moderate performance, whereas length and width showed limited performance ($R^2 \leq 0.08$), despite strong phenotypic correlations between length and width and thousand-kernel weight ($r = 0.63$ and 0.78, respectively). Feature importance analysis revealed that thousand-kernel weight showed localized importance near ~660, ~950, ~1140, and ~1900 nm, whereas aspect ratio and circularity showed broader importance across 400–2450 nm. This suggests that spectral associations with shape traits were not simply attributable to kernel size or mass. Overall, kernel morphology may represent a potential physical confounding factor in whole-grain spectral analysis and should be considered when developing and interpreting reflectance-based grain-quality models.

1. Introduction

Wheat is one of the most important staple crops worldwide, providing a major source of calories and protein for a large proportion of the global population. The physical characteristics of wheat kernels are critical determinants of kernel quality and end-use performance. Wheat kernel shape and size directly affect kernel weight, packing efficiency, and milling behavior, and are closely associated with germination potential and early seedling vigor (Schierenbeck et al., 2021). Variations in kernel morphology can arise from genetic differences, environmental conditions (Yabwalo et al., 2018), and management practices (Dupont and Altenbach, 2003). Morphological traits commonly used to characterize wheat kernels include kernel length, width, projected area, and aspect ratio, defined as the ratio of kernel length to width. These traits provide quantitative descriptors of kernel shape and size and are frequently used in kernel classification, breeding programs, and quality assessment (Wang et al., 2023). More specifically, aspect ratio and proportional shape metrics have been widely used to classify wheat into market classes (Neuman et al., 1987; Symons and Fulcher, 1988), distinguish between ancient and modern wheat species (Goriewa-Duba et al., 2018; Martín-Gómez et al., 2019; Wang et al., 2023), and evaluate grain physical quality (Sharma et al., 2021). Furthermore, aspect ratio and roundness directly affect bulk packing efficiency, spatial arrangement, and pore volume within storage containers (Ramaj et al., 2024). Additional shape descriptors such as circularity, solidity, compactness, and density can be used to distinguish between well-developed and defective or shriveled kernels (Sharma et al., 2021), assess differences in kernel development and appearance across varieties and species (Goriewa-Duba et al., 2018), and provide insights into grain quality and physical properties such as bulk test weight (Yabwalo et al., 2018).

* Corresponding author.
E-mail address: simon.futerman@mail.huji.ac.il (S.I. Futerman).

https://doi.org/10.1016/j.jfca.2026.109633
Received 6 August 2026; Received in revised form 25 October 2026; Accepted 26 October 2026
Available online 27 October 2026
0889-1575/© 2026 The Authors. Published by Elsevier Inc. This is an open access article under the CC BY license (http://creativecommons.org/licenses/by/4.0/).

Non-destructive, near real time, approaches for assessing wheat kernel quality are increasingly important, as they allow rapid and repeatable evaluation of large numbers of samples without damaging the kernels. One widely used non-destructive technique is the acquisition of Red Green Blue (RGB) images, which enables the extraction of wheat morphological traits from digital images (Hu and Zhang, 2021; Zhihong et al., 2016). This approach provides a practical and high-throughput means of characterizing kernel morphology and evaluating variation in kernel traits. Kernel geometric features, including length, width, projected area, and shape descriptors have been quantified with RGB images (Martín-Gómez et al., 2019; Sharma et al., 2021). However, in many of these studies, calibration or validation objects are not included in the images and thus structural uncertainty remains high. Since several factors can significantly affect image acquisition quality, such as camera orientation, distance from the object, and focus-related distortions, particularly toward the edges of the image, the reliability and accuracy of the measured morphological traits may be compromised.

Another non-destructive approach for assessing wheat kernels is the use of reflectance spectroscopy, which can be applied to both bulk kernel samples and individual kernels, using both point spectroscopy and spectral imaging systems. Kernel quality measurements using spectroscopic approaches have been conducted for several decades (Osborne, 1987, 1984). Reflectance spectroscopic techniques measure radiation reflected from the kernel surface, resulting from the combined effects of light scattering and absorption during the interaction of light with the kernel. These processes are governed by the real and imaginary components of the complex refractive index. The acquired spectrum therefore contains information related to both the biochemical composition (absorption) and physical structure (scattering) of the kernel. In conventional NIR spectroscopy of ground flour, physical particle size is recognized as a factor that can affect light scattering and, consequently, the performance and interpretation of chemical calibrations (Osborne, 1987). In unground whole grains, differences in kernel geometry may similarly contribute to the measured spectral response through physical scattering effects. Spectral methods can therefore provide rapid, non-destructive estimates of kernel quality parameters, although the measured spectral response may reflect both compositional and physical characteristics.

Spectral information in the visible and near-infrared regions (400–2500 nm) is particularly informative for kernel analysis (Du et al., 2022). Reflectance in the visible range (approximately 400–700 nm) is mainly related to pigment content and surface characteristics, while the near-infrared region (approximately 700–1100 nm) contains information about the cellular structure within the kernel (Liu et al., 2025). The short-wave-infrared region (approximately 1100–2500 nm) contains absorption features associated with organic molecules such as starch, protein, oil and cellulose. Water molecules are active at around 1400 and 1900 nm. One of the main uses of spectroscopy is the prediction of kernel protein content (Delwiche, 1998; Delwiche and Hruschka, 2000; Du et al., 2022; Williams, 2020; Zhang et al., 2019). Protein content in wheat kernels is primarily inferred from absorption features associated with N-H bonds in the near-infrared region, with strong predictive information commonly found in the 1100–1400 nm range corresponding to second overtone and combination bands, but also at additional wavelength around 2000 nm. With appropriate calibration and data processing, spectral measurements can be used to extract meaningful indicators of kernel composition and morphology, supporting both research and practical applications in quality assessment and phenotyping.

While highly valuable information can be derived from spectral measurements in the absorbance mode, studies often report that wheat kernel morphology can significantly affect spectral results due to the interaction between the real and imaginary parts of the complex refractive index (Delwiche, 1998; Wang et al., 1999). This highlights the need to account for spectral changes caused by wheat kernel physical, rather than chemical, attributes. Evidence from near-infrared hyperspectral imaging supports the assumption that kernel morphology affects spectral results (Delwiche et al., 2021a, 2021b; Kartakoullis et al., 2025; Manley et al., 2012). Consequently, unaccounted variation in kernel geometry may represent a potential physical confounding factor in non-destructive whole-grain composition models. However, few studies have systematically evaluated the relationship between kernel morphology and bulk spectral reflectance using spatially calibrated imaging alongside point spectroscopy.

Therefore, the main aim of this study is twofold:

a. Develop a robust and calibrated method of measuring wheat kernel morphology with RGB images, captured via standard portable devices.
b. Examine the effect of wheat kernel morphology obtained from processing RGB images on the spectral signature measured by a spectrometer, evaluating its potential role as a physical confounding factor in intact-kernel spectroscopic analysis.

2. Materials and methods

2.1. Experimental setup and wheat kernel collection

Kernel samples were obtained from a controlled glasshouse experiment to establish a dataset with high morphological and spectral diversity. Briefly, wheat was grown in sandy soil amended with compost (control) and subjected to four distinct contaminant treatments: total petroleum hydrocarbons (TPH), salinity, microplastics, and nitrogen overapplication. While these treatments successfully induced substantial variability in plant development, yield, and physical grain architecture, evaluating the specific impacts of these soil conditions was outside the scope of this study. The samples were utilized solely as a source of variable phenotypic material. Kernels were harvested upon reaching full maturity, between 91 and 95 days after sowing (DAS). A total of 85 batch samples were collected, with each batch representing a distinct biological replicate harvested from an individual plant. For each plant, all harvested kernels were dried together, and a representative subsample of approximately 100–200 kernels was extracted for subsequent RGB imaging and spectral analysis, ensuring complete sample independence across all 85 batches.

2.2. Red Green Blue (RGB) image acquisition

To ensure accurate and reproducible extraction of kernel morphological parameters from RGB imagery, a standardized data acquisition protocol was established. Images were captured using an iPhone 11 smartphone camera mounted above the imaging platform at a fixed height of approximately 11 cm (Fig. 1). The integrated camera flash was enabled for all acquisitions to ensure consistent illumination and to minimize inter-kernel shadowing effects. Kernels were manually distributed on a matte white paper and spread to prevent touching and overlap.

Between imaging sessions, the phone was moved and replaced in the holder, which introduced slight variation in camera tilt angle and spatial positioning. As no corrections for length distortion were applied, an additional calibration procedure was implemented to minimize measurement variability arising from these differences. High-precision calibration and validation metal balls with known diameters of 2 and 5 mm, produced in accordance with international standard (DIN 5401) were integrated directly into the imaging field. The aim of adding these balls into each image, was to calibrate and validate each image with objects of a known size. The white background paper upon which the kernels were spread contained nine red squares on the perimeter and the middle of the paper on which 2 mm calibration balls were placed. Additionally, eight validation balls (four 2 and four 5 mm balls) were placed randomly in each image between the kernels to provide internal

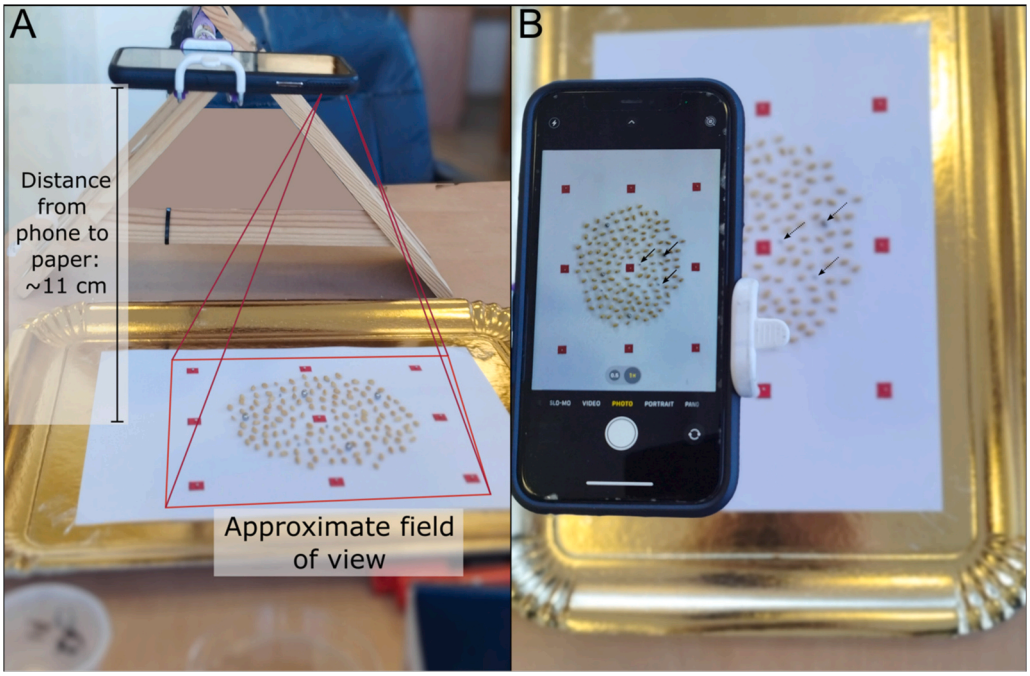

Fig. 1. Red Green Blue (RGB) image acquisition setup. A- Top view of an iPhone 11 camera was used at nadir position with flash light enabled in all images at a height of around 11 cm. Metal calibration balls with known radius (2.0 mm) were placed in the red squares, and kernels and validation balls (5.0 mm) were randomly spread across the cameras' field of view, without overlap. B- Side view of kernels and calibration and validation balls, as seen on the camera. Black arrows indicate position of some of the validation balls.

validation framework for spatial measurement accuracy across the entire field of view.

2.3. Red Green Blue image processing

All images were analyzed using a custom Python script based on the OpenCV and NumPy libraries. Images were processed individually in a batch workflow.

First, spatial calibration was performed using the calibration balls (2 mm) situated on the fixed red anchor squares (Fig. 2 A,C). The red regions were detected using a red dominance color index (Eq. 1) which highlights pixels where red intensity exceeds green and blue.

$$R - \frac{G + B}{2} \tag{1}$$

Where R, G and B represent reflectance at the red, green and blue bands, respectively. A threshold based on this index was generated and produced a binary mask of red areas, followed by morphological filtering to remove noise and connect fragmented regions. External contours were then identified, and candidate calibration objects were filtered by area, circularity (> 0.6), and expected diameter range (26–40 pixels). Within each selected region, the object diameter was estimated using the minimum enclosing circle. The localized pixel-to-millimeter conversion factor (mm px^{-1}) was calculated as the ratio between the known ball diameter to the mean detected pixel diameter, and the associated standard deviation was retained as a calibration uncertainty metric.

After the establishment of the calibration parameters, the non-target regions were excluded by masking red objects, using color index thresholding and morphological opening. Kernels in the remaining image were detected by converting the image to grayscale, smoothing with a Gaussian filter to suppress high-frequency reflections from the surface, and using edge-detection with the Canny operator (Fig. 2 B,D). Morphological dilation and erosion were applied to improve contour continuity. External contours were extracted and filtered by minimum area. Contours were retained only if morphological values fell within biologically plausible ranges (e.g., Feret diameter 1.75–9.00 mm; true width 1.5–5.00 mm). The validation balls (2 and 5 mm), that were positioned at random locations within the imaging area, were processed together with the kernels using the same detection and measurement pipeline. The diameters of all validation balls were extracted from their detected outlines and compared with their true standard dimensions. Measurement accuracy and consistency were assessed across images.

2.4. Morphological traits and thousand kernel weight estimation

Morphological traits of each detected kernel were derived from its contour following spatial calibration and using the equations presented in Table 1 (Goriewa-Duba et al., 2018). The axis-aligned bounding rectangle was used to estimate kernel width, which were converted from pixels to millimeters using the image-specific calibration factor (derived from the measured calibration balls). Kernel's area was calculated from the contour and additionally from a filled binary mask to obtain an improved estimate based on the exact number of pixels enclosed by the object. The shape was quantified using circularity, computed from contour area and perimeter. Kernel's width was calculated as a geometry-independent measure, using the span of contour points projected onto the direction perpendicular to the major axis of the minimum-area rotated rectangle. The maximum Feret diameter, defined as the largest distance between any two points on the convex hull, was computed to represent kernel length. All pixel-based measurements were then converted to millimeters using the image-specific calibration factor, derived from the calibration balls. Following image acquisition, the kernels from each batch were weighed to determine total batch mass. 1,000-kernel weight was then calculated by combining this measured mass with the image-derived kernel count, providing a mass-based physical parameter alongside the 2D geometric shape descriptors.

2.5. Spectral measurements

Spectral reflectance data for wheat kernels were acquired using an ASD FieldSpec 4 Hi-Res spectrometer, equipped with a contact-probe

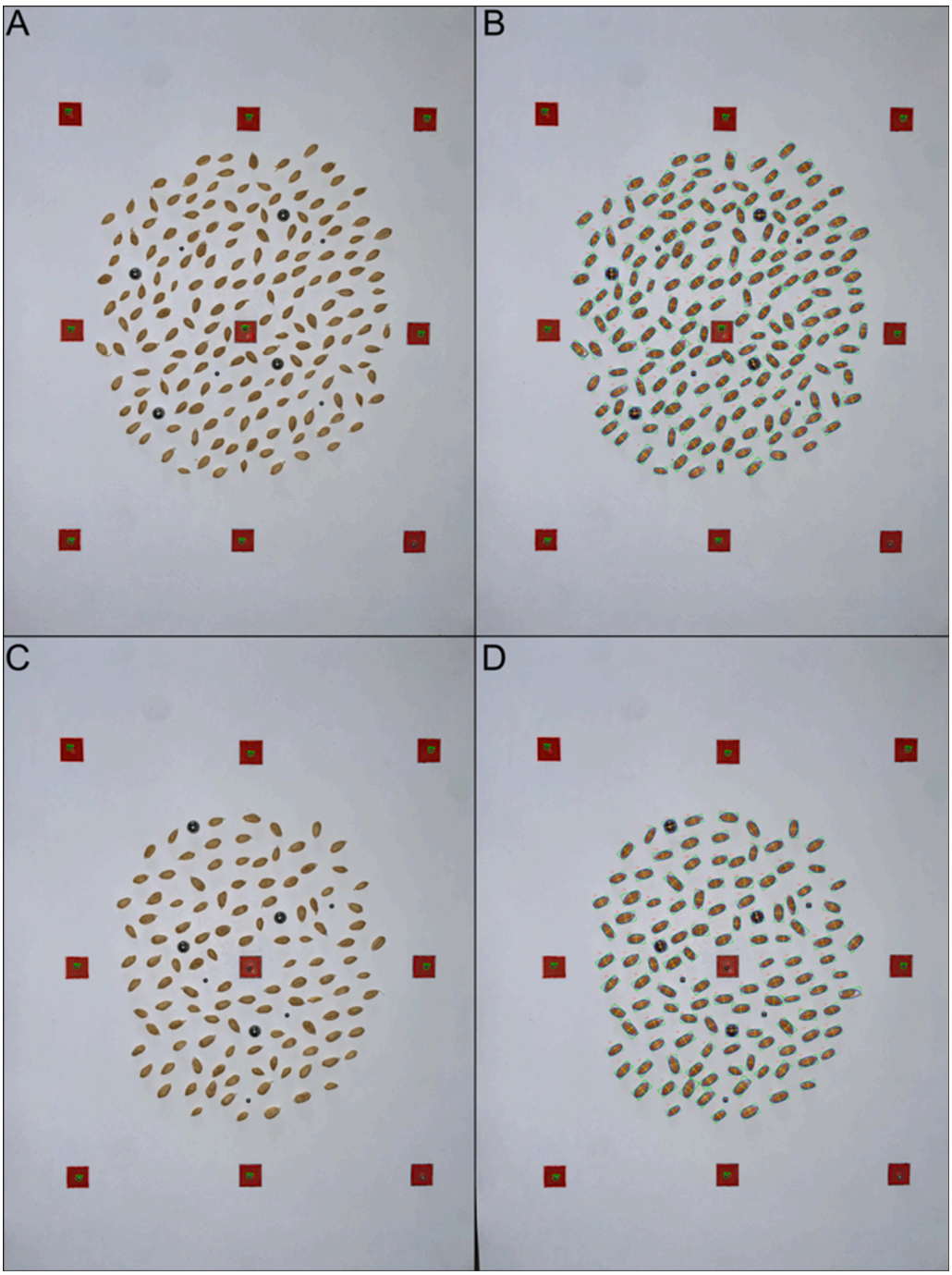

Fig. 2. A Red Green Blue (RGB) image demonstrates an example of calibration metal ball detection, indicated by green circles in panels A and C, and the subsequent detection of kernels and validation balls in panels B and D from two batches of kernels imaged. In panels B and D, green outlines indicate the kernel perimeter, red lines represent kernel length, and yellow lines denote kernel width.

assembly, following a standardized measurement protocol (Fig. 3). Measurements were conducted on the same kernel batches, used to capture RGB images. Prior to any spectral measurement session, the ASD spectrometer was warmed up for 60 min and the illumination bulb for 30 min according to the IEEE P4005 protocol (Ben Dor et al., 2024). Firstly, the optimization and calibration were performed using a Spectralon © white reference panel. A container painted black and covered with a low-reflectance black cloth was used in all measurements to minimize stray light and background reflection. The spectral properties of both the container lid and the cloth were measured prior to analysis to confirm negligible reflectance. Kernels from each batch were placed in the container and measured (Fig. 3). Each kernel batch was measured four times. Between replicate measurements, the kernels were thoroughly mixed and poured again into the measurement container to minimize the effects of sample orientation, packing density, and local heterogeneity. The resulting spectra from the four replicates were averaged to produce a representative spectral curve for each kernel batch. The spectrometer was re-optimized and recalibrated, using the white reference panel, after every four kernel-batch measurements.

2.6. *Spectral modelling: ridge and partial least squares regression (PLSR)*

Spectral modelling was conducted to examine to what extent five seed morphological and physical attributes could be predicted: aspect

Table 1
Kernel morphological parameters calculated from derived RGB images.

Parameters	Characteristics	Symbol and Equation
Area	Area of kernel contour, calculated from kernel outline	$area(mm^2) = area_{px} x (\frac{mm}{pixel})^2$
Length	Maximum distance across the kernel	$Length = \max(\lvert p_i - p_j \rvert)$ p_i and p_j are two-dimensional coordinates of contour points in the image plane
Width	Kernel thickness perpendicular to its minor axis	$Width = \max(p \, x \, n) - \min(p \, x \, n)$ n: the unit vector normal to the major axis; p: contour points
Circularity	Indicates shape roundness	$\text{Circularity} = \frac{4\pi Area}{P^2}$ P: contour perimeter
Aspect ratio	Dimensionless measure of elongation	$\text{Aspect ratio} = \frac{length}{width}$

ratio, 1000-kernel weight, length, width, and circularity. Spectral reflectance data were extracted from the spectral columns of the dataset, and wavelengths between 400 and 2450 nm were retained for analysis (350–400 and 2450–2500 nm were removed to exclude noisy bands at both edges of the detector). No target-variable or spectral outlier filtering was applied in the modelling workflow. Prior to modelling, the spectral data were preprocessed using standard normal variate (SNV) transformation followed by a Savitzky-Golay (SG) first derivative. SNV was applied independently to each spectrum by centering it around its mean reflectance and scaling by its standard deviation, thereby reducing additive and multiplicative scattering effects. The SNV-transformed spectra were subsequently processed using a SG filter with a window length of 15 spectral bands, a second-order polynomial, and a first-order derivative. The resulting preprocessed spectra were used as predictor variables in all subsequent analyses.

Two regression approaches were evaluated: partial least squares regression (PLSR) and ridge regression. For each target variable, predictive performance was evaluated using a repeated random hold-out procedure consisting of 10 independent random data splits. In each iteration, the dataset was randomly divided into a training set comprising 80% of the samples and an independent held-out test set comprising the remaining 20%. The test samples were not used during model fitting or hyperparameter selection. Within each training set, five-fold cross-validation (k = 5) with shuffled folds was used to optimize model complexity. For PLSR, 1–15 latent variables were evaluated, whereas ridge regression was evaluated over a logarithmically spaced range of regularization parameters ($\alpha = 10^{-5}$ - 10^{4}). For both PLSR and ridge regression, two hyperparameter selection strategies were compared. First, the minimum mean squared error (Min-MSE) criterion selected the hyperparameter associated with the lowest mean cross-validation error. Second, the one-standard-error (1-SE) rule selected a simpler model whose cross-validation error was within one standard error of the minimum. For PLSR, the 1-SE rule selected the model with the smallest number of latent variables meeting this criterion. For ridge regression, the largest α value within the one-standard-error threshold was selected, corresponding to the strongest regularization meeting the criterion.

For each iteration, the selected PLSR and ridge regression models were refitted using the complete training subset and evaluated using the independent test subset. Model performance was quantified using the coefficient of determination (R^2) and the root mean squared error of prediction (RMSEP). The performance of four model variants was therefore compared for each target attribute: PLSR with Min-MSE selection, PLSR with 1-SE selection, ridge regression with Min-MSE selection, and ridge regression with 1-SE selection. The best-performing model variant for each target was identified according to the highest mean independent test-set R^2 across the 10 random splits. Master models were subsequently fitted to the full dataset for each target, with hyperparameters re-optimized via five-fold cross-validation using the winning selection rule. No additional predictor standardizations were applied during regression. For model interpretation, regression coefficients were extracted from the final master model for each wavelength.

Feature importance analysis was restricted to traits with adequate predictive performance, defined as a mean test $R^2 > 0.4$ across the 10 cross-validation iterations. The stability of regression coefficients across the Monte Carlo iterations was evaluated using a Jackknife-based uncertainty approach. For each wavelength i, the mean regression coefficient ($\bar{\beta}_i$) and its standard error [$SE(\beta_i)$] were calculated across model iterations. A two-tailed Student's t-statistic was then calculated as:

$$t_i = \bar{\beta}_i / SE(\beta_i)$$

Wavelengths whose regression coefficients were not statistically

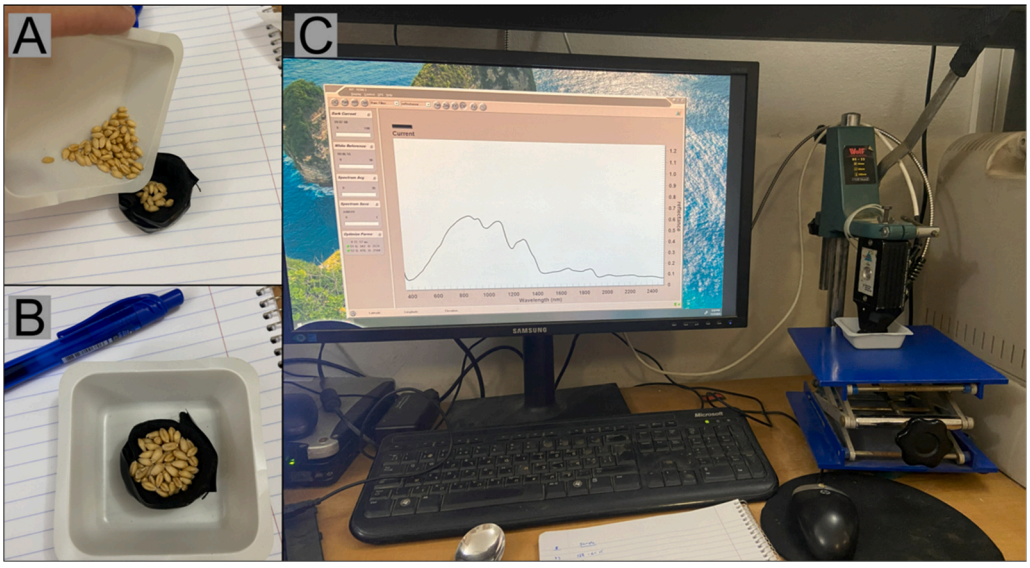

Fig. 3. Spectral measurements of wheat kernel batches. A- the kernels were poured into a container painted black and covered with a non-reflecting fabric. B- container was placed in a larger container and C- measured using a ASD FieldSpec 4 Hi-Res spectrometer, resulting in a typical wheat kernel spectral curve seen in the monitor. This process was repeated four times per batch.

stable across iterations ($p \geq 0.05$) were excluded from further analysis by setting their importance values to zero. For the remaining significant wavelengths ($p < 0.05$), the absolute regression coefficients were normalized to obtain relative feature importance:

$$I_i = |\beta_i| \; / \; \Sigma_{k=1}^{p} \, |\beta_k|$$

where p represents the total number of spectral variables. The resulting importance values were compared with the theoretical uniform importance baseline, 1/p (approximately 0.0005 for $p = 2051$).

3. Results

3.1. Calibration and validation using metal balls

In each image, nine 2 mm calibration balls were placed at fixed grid positions, while eight validation balls (four 2 mm and four 5 mm) were randomly distributed within the imaging area (Figs. 1–2). The detected pixel diameters of the calibration balls across the images are shown in Fig. 4. Across all acquisitions, the calibration balls had a mean detected diameter of 31.84 px (Fig. 4A). Mean diameters across the nine grid positions (Fig. 4B) ranged from 29.80 ± 2.63 px at the bottom-center position (Position #8) to 33.86 ± 2.28 px at the top-right position (Position #3), indicating small differences in size across the image field. A pixel-to-millimeter conversion factor was calculated separately for each image using the mean pixel diameter of the nine calibration balls.

Fig. 5 shows the relative measurement error (%) of the detected diameters compared with the nominal sizes of the 2- and 5-mm validation balls. The mean relative error was −3.06% ± 5.13% for the 2 mm balls and −5.35% ± 3.09% for the 5 mm balls. Both size classes showed a small negative bias, indicating a tendency toward slight underestimation of the true diameter. Nevertheless, the relatively small standard deviations indicate consistent measurements across the validation balls, with errors remaining within approximately 5% on average.

3.2. Morphological parameters derived from Red Green Blue (RGB) images

Image-based analysis produced a comprehensive set of kernel morphology metrics, capturing variability in kernel size and shape across treatments. As an illustrative subset of the extracted traits, kernel maximum length, measured as maximum Feret diameter, width, and aspect ratio (L/W) are presented in Fig. 6. These parameters highlight the extent of morphological variation between batches.

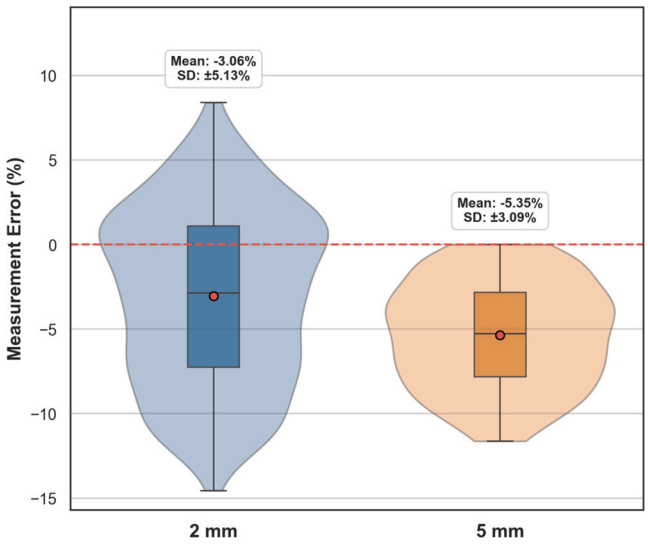

Fig. 5. Relative measurement error for the 2- and 5-mm validation balls. The dashed line represents zero error, and values show the mean ± SD for each sphere size.

Correlation analysis was conducted to examine the relationships between seed morphological traits extracted from RGB images, including length, width, aspect ratio, and circularity, and laboratory measured 1,000-kernel weight (Fig. 7). The strongest positive relationships were observed among the size-related traits. Seed length showed a moderate positive correlation with 1,000-kernel weight ($r = 0.63$, $R^2 = 0.39$), while the strongest relationship was observed between length and width ($r = 0.89$, $R^2 = 0.80$). A strong positive relationship was also observed between 1,000-kernel weight and width ($r = 0.78$, $R^2 = 0.61$), indicating that heavier kernels generally tended to be both longer and wider. In contrast, aspect ratio showed no relationship with 1,000-kernel weight ($r = 0.03$, $R^2 = 0.00$), suggesting that kernel mass was more strongly associated with absolute kernel dimensions than with their proportional shape. Circularity also showed only a weak relationship with 1,000-kernel weight ($r = 0.14$, $R^2 = 0.02$). Among the morphological traits, aspect ratio was moderately positively correlated with length ($r = 0.67$, $R^2 = 0.45$) but negatively correlated with

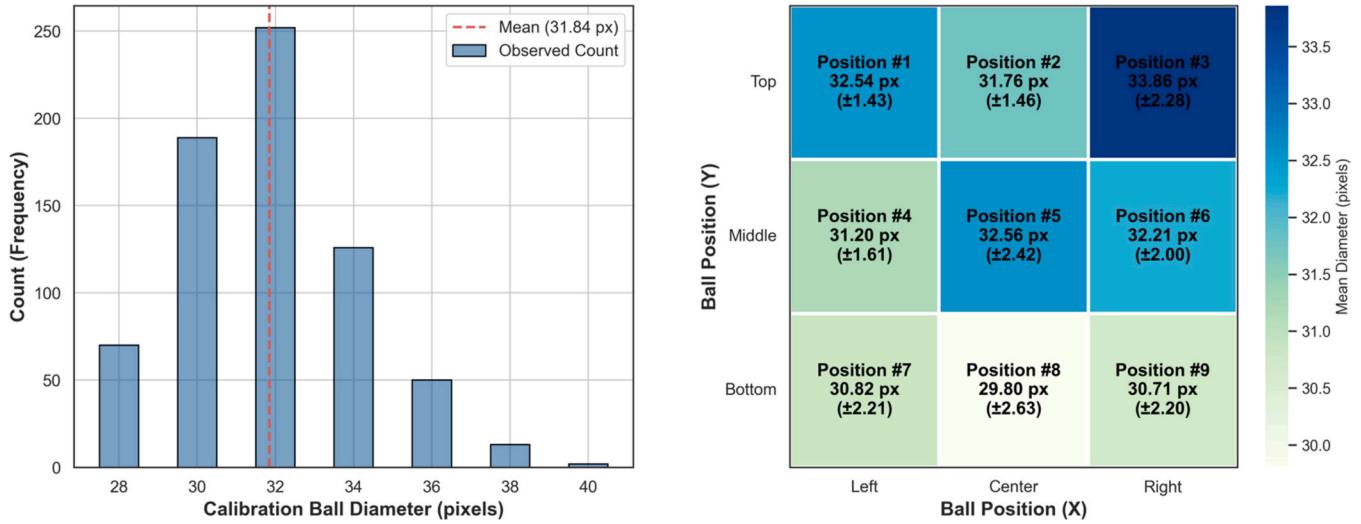

Fig. 4. Distribution of calibration ball measurements and variation across the image field. (A) Histogram showing the distribution of detected calibration ball diameters (pixels) across all images. the dashed line indicates the overall mean diameter (31.84 px). (B) Heatmap showing the mean diameter and standard deviation (mean ± SD, pixels) at nine positions within the image field. For ball position within the image, see Fig. 2.

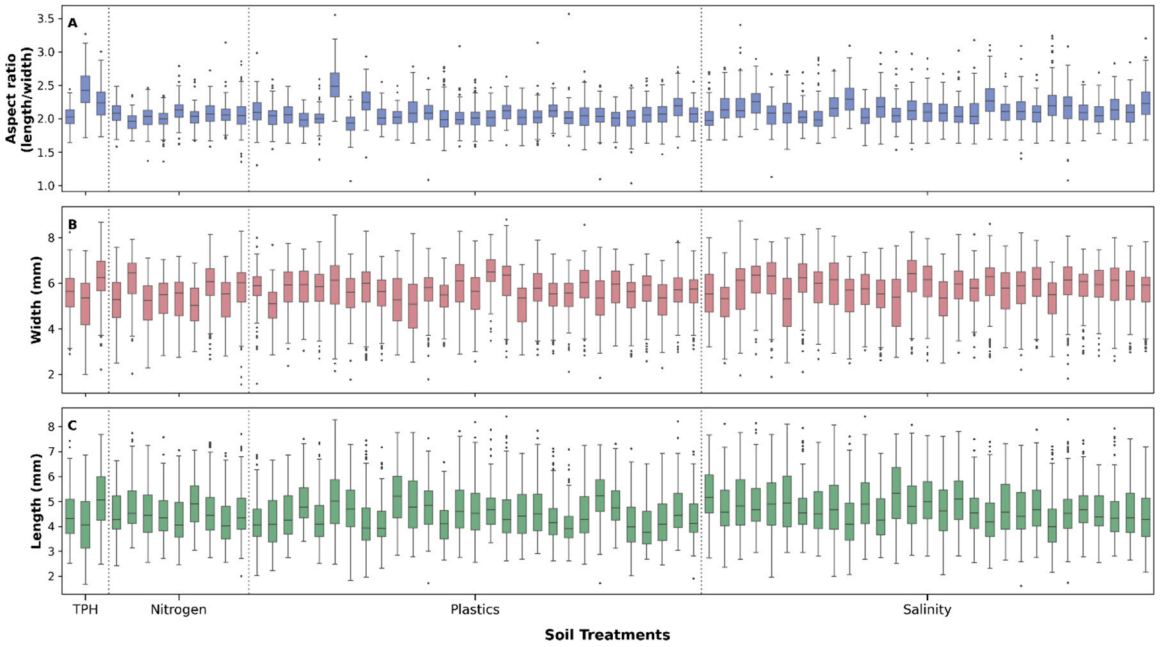

Fig. 6. Kernel aspect ratio (length/width) (A) width (mm) (B) and length (mm) (C). Each box plot represents the measurements extracted from a single image (one batch), from the different treatments indicated in the X axis.

circularity ($r = -0.43$, $R^2 = 0.19$). Circularity showed negligible relationships with both length ($r = -0.14$, $R^2 = 0.02$) and width ($r = 0.06$, $R^2 = 0.00$). Overall, the results indicate that kernel size, particularly width and length, was more strongly associated with 1,000-kernel weight than kernel shape metrics such as aspect ratio and circularity.

3.3. Spectral reflectance results

Reflectance spectra of all the kernel batches measured in this study ($n = 85$) across the 350–2500 nm wavelength range are presented in Fig. S1. The spectra show the typical increase in reflectance from the visible to the near-infrared region, followed by distinct absorption features around 970 nm, 1200 nm, 1450 nm, and ~1940 nm associated with water absorption and organic molecular bonds. The overall spectral shape is consistent across samples, while differences in overall reflectance magnitude between curves indicate variability among kernel batch samples. Prior to spectral modelling, spectral reflectance curves were examined visually as presented in Fig. 8, by looking at the association of kernel aspect ratio and 1,000-kernel weight with spectral reflectance. From a visual inspection, kernel batches with higher aspect ratios, corresponding to more elongated kernels, consistently exhibited higher overall reflectance across the visible, near-infrared, and shortwave infrared regions. In contrast, kernel batches with lower aspect ratios, representing more rounded shapes, showed comparatively lower reflectance values across the same wavelength ranges. These differences were most apparent in the near-infrared and shortwave infrared regions (1000 nm, 1700 nm), where separation between the spectral curves was more pronounced.

3.4. Spectral modelling results and feature importance

PLS and Ridge regression were conducted on preprocessed kernel reflectance spectra following standard normal variate (SNV) transformation and Savitzky-Golay first-derivative filtering. Models were evaluated across 10 cross-validation iterations, with performance metrics calculated from held-out test predictions and summarized in Table 2. Overall, Ridge regression demonstrated superior predictive performance compared to PLS for four of the five morphological traits. Predictive performance varied substantially among traits, indicating considerable differences in the extent to which the measured kernel morphological and physical properties were associated with spectral variation.

1,000-kernel weight showed the highest predictive results and the greatest generalization stability, with a mean test R^2 of 0.59 ± 0.09 and an RMSEP of 3.31 ± 0.41 g. The relatively small difference between the mean training ($R^2 = 0.73$) and cross-validation ($R^2 = 0.63$) performance further indicated a comparatively robust calibration. Among the image-derived morphological traits aspect ratio achieved a mean test R^2 of 0.57 ± 0.15 and an RMSEP of 0.06 ± 0.01, while circularity achieved a mean test R^2 of 0.46 ± 0.25 and an RMSEP of 0.02 ± 0.00. In contrast, seed length and seed width produced mean test R^2 values of only 0.06 ± 0.12 and 0.08 ± 0.2, respectively, indicating that robust predictive models could not be established for these traits. Overall, 1,000-kernel weight produced the strongest and most consistent results, followed by aspect ratio and circularity, whereas seed length and width showed limited predictive capability.

Spectral importance profiles varied across the three traits relative to the uniform baseline (Fig. 9). In general, the diagnostic profiles showed a clear distinction between the traits, with 1,000-kernel weight characterized by a small number of confined diagnostic spectral regions, whereas aspect ratio and circularity mean were associated with importance distributed across a broader range of wavelengths. 1,000-kernel weight had several localized peaks concentrated around 660 nm, 1140 nm and 1900 nm. Large regions of the spectra showed little or no importance. In contrast, aspect ratio and circularity mean displayed more broadly distributed importance profiles across the entire 400–2450 nm range. For aspect ratio, wavelengths exceeding the uniform baseline occurred across multiple spectral regions, with pronounced peaks in the VIS, around 550–650 nm and in the NIR, 1100–1200 nm, as well as at around 2300–2400 nm. Circularity mean showed a similar distributed pattern, although its highest importance values were concentrated mainly in the visible region, around 550–600 nm, with additional localized peaks near 950 nm and 1100 nm.

4. Discussion

The aim of this study was to develop a robust, calibrated RGB

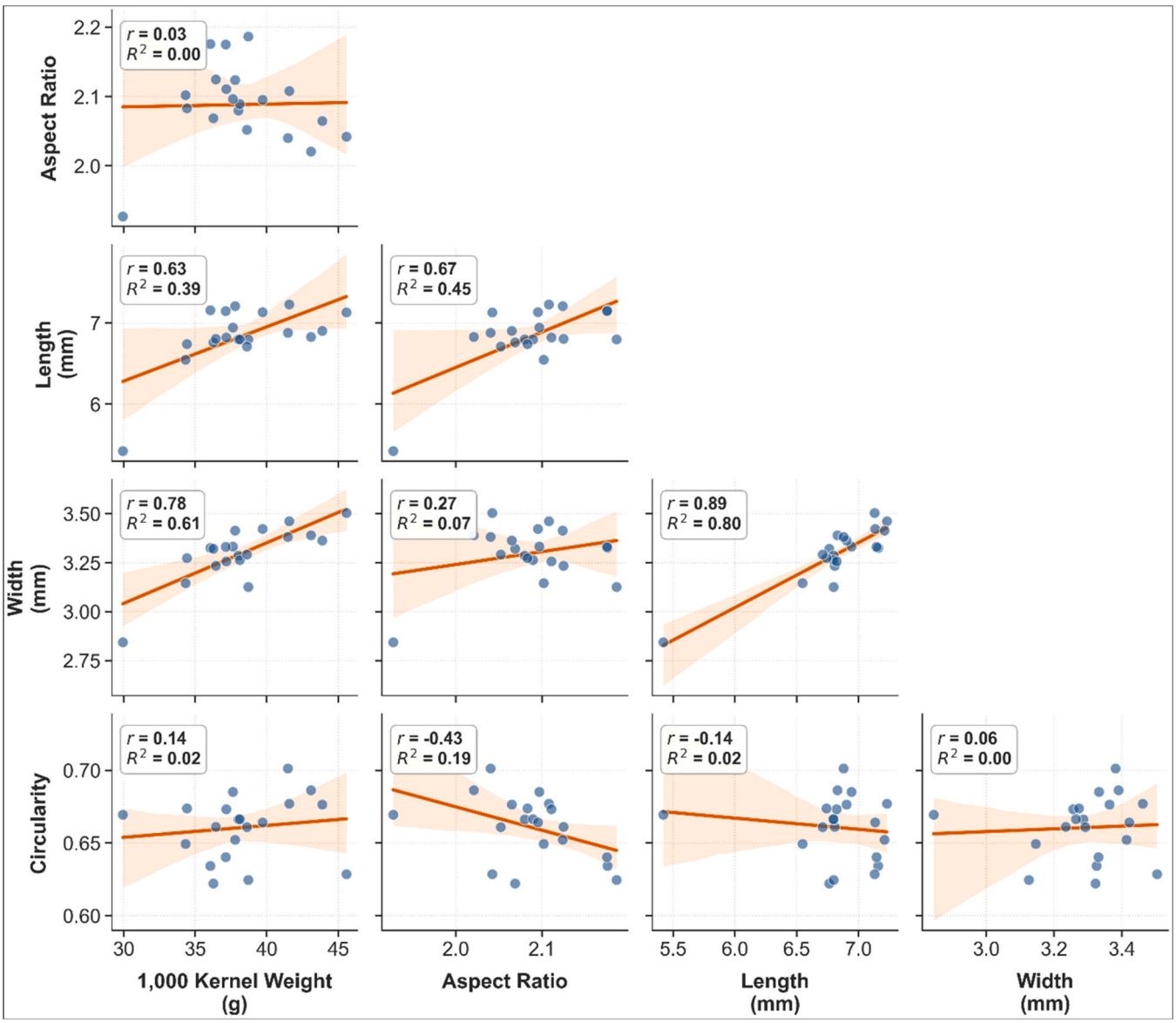

Fig. 7. Correlation between several morphology traits measured from RGB images (width, length, aspect ratio, circularity) and 1,000-kernel weight.

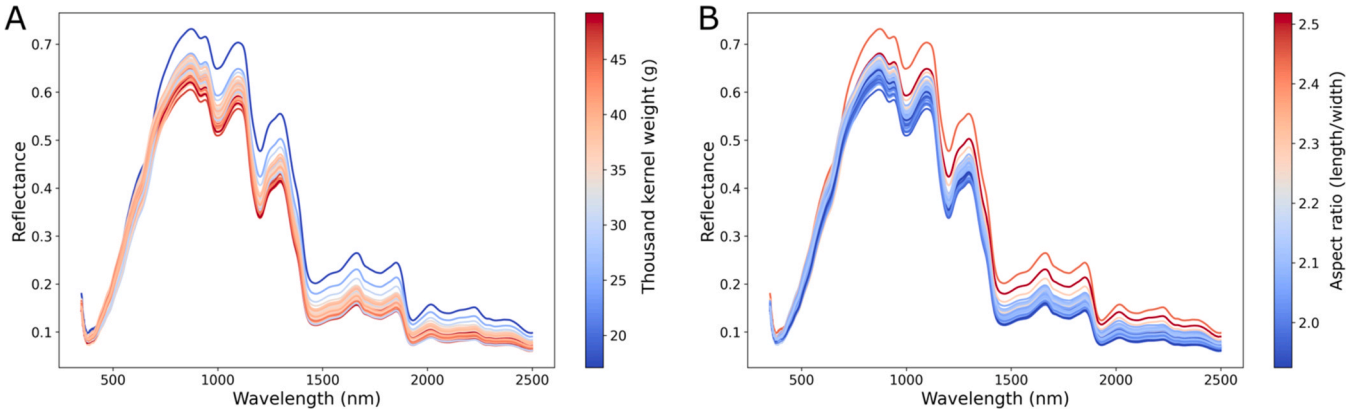

Fig. 8. Spectral reflectance of all wheat kernel samples measured in the study, with curves colored according to (A) thousand kernel weight and (B) aspect ratio.

imaging method for measuring wheat kernel morphology and to examine how morphological traits are associated with the spectral signatures across the 350–2500 nm range.

To address these aims, RGB images were acquired under a protocol with metal balls, with a known diameter, as calibration and validation objects, using a simple and available smartphone camera (iPhone 11)

Table 2
Model prediction results of five seed morphological attributes.

Attribute	Model	Train R^2	CV R^2	Test R^2	RMSEP
1,000-kernel weight	Ridge	0.73 ± 0.07	0.63 ± 0.03	0.59 ± 0.09	3.31 ± 0.411
Aspect Ratio	Ridge	0.83 ± 0.03	0.53 ± 0.07	0.57 ± 0.16	0.06 ± 0.01
Circularity	Ridge	0.7 ± 0.07	0.5 ± 0.07	0.46 ± 0.24	0.02 ± 0.00
Length	Ridge	0.3 ± 0.07	0.10 ± 0.03	0.06 ± 0.12	0.36 ± 0.04
Width	PLS	0.33 ± 0.06	0.26 ± 0.06	0.08 ± 0.2	0.18 ± 0.02

(Figs. 1–2). Although the feasibility of using RGB images to derive kernel morphological traits has been demonstrated previously (Goriewa-Duba et al., 2018; Martín-Gómez et al., 2019) the method developed here was designed to reduce errors caused by lighting conditions, camera positioning and lens distortions (Halcro et al., 2020). The use of calibration objects enables normalization across images and acquisition sessions, while validation objects provide an internal check on measurement accuracy. In this study, we used 2 mm balls for calibration, and 2- and 5-mm balls for validation (Figs. 1–2). The inclusion of the calibration balls allowed image-specific calibration and helped account for spatial variation in pixel scale across the field of view, with measured sphere diameters ranging from 29.80 to 33.86 px around an overall mean of 31.84 px (Fig. 4). Independent validation balls, randomly positioned in each image, further demonstrated the consistency of the measurements, with relative errors of −3.06% ± 5.13% for 2 mm spheres and −5.35% ± 3.09% for 5 mm spheres (Fig. 5). The low errors obtained using this method demonstrate that the workflow successfully accounted for differences in image acquisition sessions and between images (Figs. 4–5). This is particularly important for low-cost phenotyping workflows, where variability in acquisition geometry and illumination can substantially reduce reproducibility between datasets. Therefore, we suggest that future studies should incorporate calibration and validation objects in image acquisition protocols.

Overall, large variability in kernels' size was observed in this study, as expected, because kernels were collected from a controlled glasshouse experiment with different soil contaminant applications. The observed variation in kernel morphological traits was useful for downstream assessment of the relationships between the morphological traits and the spectral reflectance. The spectral modelling results demonstrate that 1000-kernel weight was the most successfully predicted attribute (*Test R^2 = 0.59 ± 0.09*) (Table 2), showing relatively low variation across iterations and a comparatively small reduction from training to test performance. Conversely, length and width showed limited spectral predictability (*Test R^2 = 0.06 ± 0.12* and R^2 = *0.08 ± 0.20, respectively*), (Table 2). This occurred despite their strong phenotypic correlations with 1000-kernel weight (*r = 0.63 and 0.78*, respectively) (Fig. 7). This

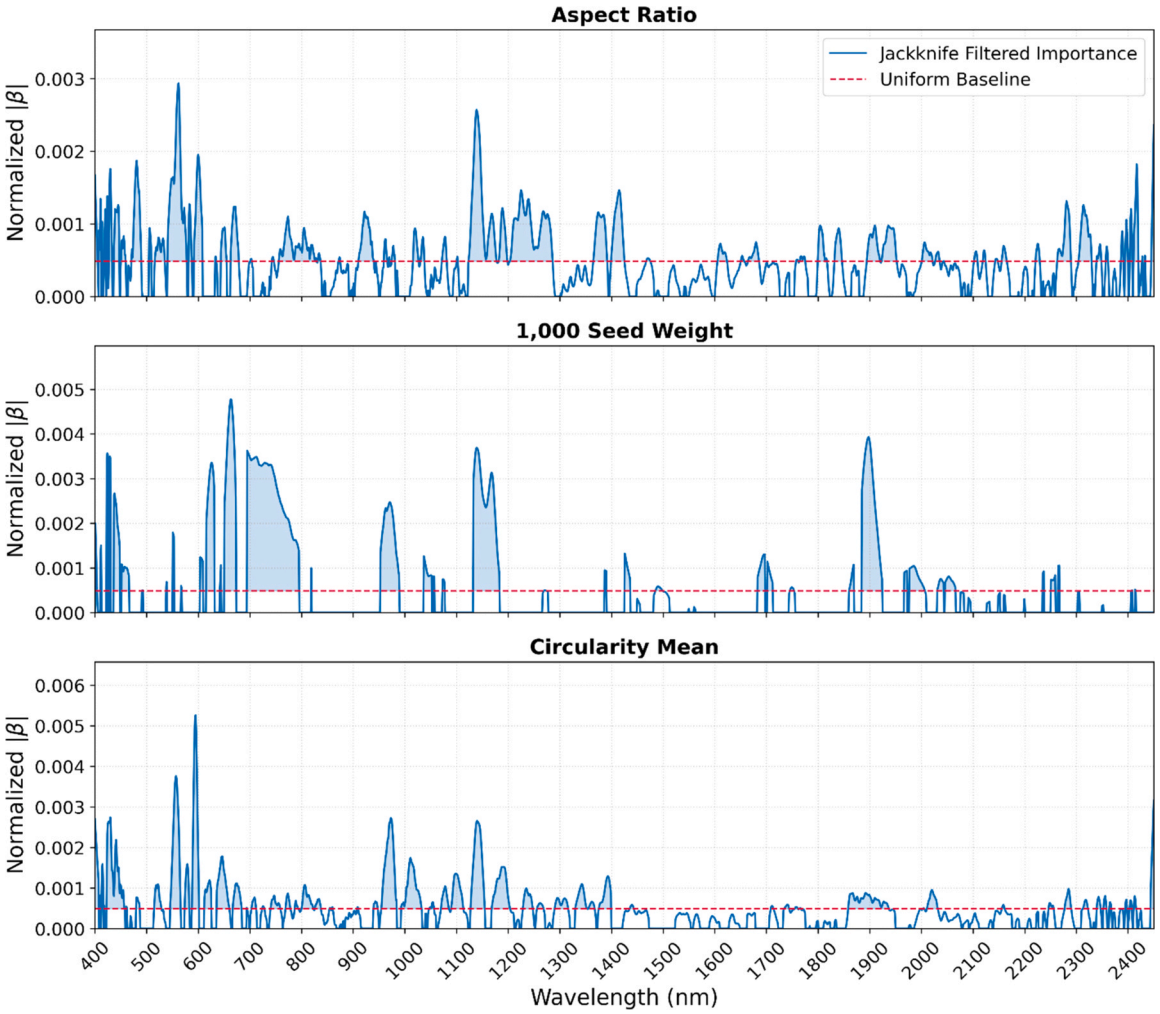

Fig. 9. Diagnostic spectral importance profiles across the VIS-NIR-SWIR spectrum (400–2450 nm) for aspect ratio, 1000 kernel weight and circularity. Panels display normalized jackknife-filtered coefficient magnitudes (solid blue lines). The red dashed line is the uniform baseline threshold. Blue shaded areas indicate spectral bands where coefficients remained stable across the iterations and variable importance exceeds the uniform baseline.

divergence indicates that whereas 2D image-based measurements characterize external kernel dimensions, kernel mass also reflects properties such as thickness, tissue density, and chemical composition that are not captured by these linear measurements. The feature importance profile provides further support for this interpretation (Fig. 9), with 1000-kernel weight characterized by relatively narrow regions of high importance near ~950, ~1140, and ~1900 nm. These regions coincide with established O-H and C-H related absorption features associated with water and organic constituents, including carbohydrates and lipids. The concentration of predictive importance around these NIR-SWIR regions is therefore consistent with a contribution of kernel composition and bulk physical properties to the spectral prediction of 1000-kernel weight. However, because reference chemical traits were not directly quantified in this study, these spectral importance profiles represent statistical model weighting rather than direct evidence of specific biochemical mechanisms, and require further validation with reference chemistry.

A contrasting pattern emerged for the geometric shape traits. Aspect ratio and circularity exhibited moderate spectral predictability (*Test* $R^2 = 0.57 \pm 0.16$ and 0.46 ± 0.24, respectively) (Table 2), despite their weak phenotypic relationships with 1000-kernel weight ($r = 0.03$ *and* 0.14, respectively) (Fig. 7). Thus, spectral information associated with kernel shape was not simply a consequence of variation in kernel mass. Instead, these relationships may arise indirectly through the influence of kernel geometry on measured reflectance, including effects associated with surface curvature, orientation, shading, and light scattering. Aspect ratio showed a broadly distributed importance pattern spanning the spectral range (400–2450 nm), with contributions across multiple spectral regions rather than a small number of localized absorption features (Fig. 9). This distributed spectral response is consistent with a more complex and indirect relationship between kernel geometry and reflectance and may partly explain the greater reduction from training to test performance (*Train* $R^2 = 0.83 \pm 0.03$; *Test* $R^2 = 0.57 \pm 0.16$). Surface appearance, pigmentation, curvature, and shading may contribute to this relationship, although the individual mechanisms cannot be separated using the present data.

Taken together, the results highlight the complementary information provided by RGB imaging and spectral reflectance. The RGB measurements directly quantified external two-dimensional kernel morphology, whereas spectral measurements captured spectral variation associated with both kernel composition and optical properties influenced by surface geometry. The coupling of these two methods provides a more comprehensive understanding of kernel morphological and spectral variation. This finding may partially explain inconsistencies or unexplained variance commonly observed in chemometric models developed from kernel reflectance data (Mahato et al., 2026). Similar structural effects are well known in soil spectroscopy, where particle size and shape significantly influence reflectance (Ben-Dor, 2002; Sadeghi et al., 2018). In the case of kernel batch spectral measurements, kernel shape affects surface curvature, orientation, and packing arrangement, all of which influence light scattering and shadowing within a batch sample.

These observations have important implications for spectral modelling. Reflectance-based models are widely used to estimate biochemical constituents (e.g., protein, moisture). However, the demonstrated association of morphology suggests that structural variability may act as a confounding factor, introducing systematic variation unrelated to the target variable. Indeed, the effect of kernel curvature and physical traits has previously been demonstrated. For example, Wang et al., (1999) measured reflectance of single wheat kernels and showed that kernel weight, ranging from 17.6 to 57.2 mg, affected reflectance in the visible and near-infrared spectral regions. Another study reported an offset in the overall magnitude of reflectance caused by kernel mass alone in single kernel spectral measurements (Delwiche, 1998). The authors compared kernels with the same mass and different protein content, and the same protein content and mass, and showed that the offset caused by kernel mass was nearly as large as that caused by differences in protein content, in the 1110–2498 nm spectral region. Manley et al., (2012) found that kernel curvature contributed most to spectral variation in near-infrared hyperspectral imaging. In order to address this issue, incorporating morphological descriptors into predictive models, may allow the model to disentangle structural and compositional contributions. Incorporating RGB-derived morphological traits into the modelling framework could therefore improve predictive performance by providing complementary information for spectral modelling.

Typically, to obtain chemical attributes from kernels, the samples are ground, thereby eliminating scattering effects associated with kernel structure. This preprocessing step minimizes structural influences on reflectance and enables a more direct assessment of chemical composition. Based on the findings of this study, we recommend acquiring reflectance and RGB measurements prior to grinding in order to preserve the geometrical information of the kernels. Such structural information may provide valuable indicators of kernel quality before the milling process converts the kernels into powder. Furthermore, integrating pre-grinding morphological measurements with post-grinding chemical analyses may help disentangle structural and compositional contributions to spectral signals, potentially improving the robustness and interpretability of predictive models.

Overall, the results highlight that the output of spectral measurements of wheat kernel batches reflects a combination of morphological and biochemical parameters, and that these contributions are not easily separable without additional information. This has important implications for the interpretation of spectral datasets, particularly when spectral measurements are used to infer biochemical composition without accounting for structural variation. The demonstrated link between morphology and reflectance provides a potential mechanistic explanation for part of the variability observed in spectral data. These findings suggest that future modelling efforts should consider integrating multiple data sources and explicitly accounting for structural variability, rather than relying solely on spectral information. However, it should be noted that the present study was conducted on one wheat cultivar alone (Fielder), and broader genetic diversity may introduce additional morphological and spectral variability. Future studies should further evaluate these relationships across different wheat cultivars, environmental conditions, and imaging configurations to determine the generalizability of the observed effects.

5. Conclusions

In conclusion, this study demonstrates significant optical and statistical associations between wheat kernel morphology and bulk-sample spectral reflectance across the 400–2450 nm range. By integrating calibrated smartphone imaging with spectroscopy, the analysis revealed different spectral patterns for mass and geometric traits. 1000-kernel weight (R^2 test $= 0.59 \pm 0.09$) was associated with more localized regions of spectral importance near 660, 950, 1140, and 1900 nm, whereas aspect ratio (R^2 test $= 0.57 \pm 0.16$) and circularity (R^2 test $= 0.46 \pm 0.24$) showed broader spectral importance across 400–2450 nm range. In contrast, length and width showed limited spectral predictability (R^2 test ≤ 0.08), despite strong phenotypic correlations with 1,000-kernel weight, indicating that the shape-related relationships were not simply a reflection of kernel size or mass.

These findings indicate that kernel morphology represents an important physical component of the variation observed in whole-grain spectroscopic signatures and may act as a structural confounding factor in non-destructive composition calibrations (e.g., protein, moisture). Analogous to particle-size light scattering in ground-flour NIR analysis, structural characteristics such as shape, surface curvature, and bulk packing arrangement may contribute to physical spectral variation unrelated to chemical target properties. Incorporating calibrated morphological measurements into intact-grain chemometric workflows could provide an additional means of accounting for physical sources of spectral variation and may help explain or reduce variability in rapid

grain-quality prediction models.

CRediT authorship contribution statement

Simon Ian Futerman: Writing – original draft, Methodology, Investigation, Formal analysis, Data curation, Conceptualization. **Eyal Ben Dor:** Writing – review & editing, Supervision, Investigation, Funding acquisition, Conceptualization. **Nir Sade:** Writing – review & editing, Funding acquisition, Conceptualization. **Israel Oren:** Writing – review & editing, Data curation. **Antonios Morellos:** Writing – review & editing. **Abdul Mounem Mouazen:** Writing – review & editing.

Declaration of Generative AI and AI-assisted technologies in the manuscript preparation process

During the preparation of this work the author(s) used ChatGPT (GPT 5.5) to assist with writing the code for the RGB image analysis and the kernel morphological trait estimation. After using this tool/service, the author(s) reviewed and edited the content as needed and take(s) full responsibility for the content of the published article.

Declaration of Competing Interest

The authors declare that they have no known competing financial interests or personal relationships that could have appeared to influence the work reported in this paper.

Acknowledgments

Authors acknowledge the financial support received from WHEAT-WATCHER project, funded by the European Union under the Horizon Europe program and Swiss State Secretariat for Education, Research and Innovation (SERI), grant agreement No. 101156480.

Appendix A. Supporting information

Supplementary data associated with this article can be found in the online version at doi:10.1016/j.jfca.2026.109633.

Data availability

Data will be made available on request.

References

Ben Dor, E., Karyotis, K., Chabrillat, S., Schmid, T., 2024. Standardization and Protocol Development for Soil Spectral Reflectance in Laboratory and Field Settings: An Overview of IEEE SA P4005 Activity, in: IGARSS 2024 - 2024 IEEE International Geoscience and Remote Sensing Symposium. pp. 268–270. https://doi.org/10.1109/IGARSS53475.2024.10641689.

Ben-Dor, E., 2002. Quantitative remote sensing of soil properties.

Delwiche, S.R., 1998. Protein content of single kernels of wheat by near-infrared reflectance spectroscopy. J. Cereal Sci. 27, 241–254. https://doi.org/10.1006/jcrs.1997.0165.

Delwiche, S.R., Baek, I., Kim, M.S., 2021a. Effect of curvature on hyperspectral reflectance images of cereal seed-sized objects. Biosyst. Eng. 202, 55–65. https://doi.org/10.1016/j.biosystemseng.2020.11.004.

Delwiche, S.R., Baek, I., Kim, M.S., 2021b. Does spatial region of interest (ROI) matter in multispectral and hyperspectral imaging of segmented wheat kernels? Biosyst. Eng. 212, 106–114. https://doi.org/10.1016/j.biosystemseng.2021.10.003.

Delwiche, S.R., Hruschka, W.R., 2000. Protein content of bulk wheat from near-infrared reflectance of individual kernels. Cereal Chem. 77, 86–88. https://doi.org/10.1094/CCHEM.2000.77.1.86.

Du, Z., Tian, W., Tilley, M., Wang, D., Zhang, G., Li, Y., 2022. Quantitative assessment of wheat quality using near-infrared spectroscopy: a comprehensive review. Compr. Rev. Food Sci. Food Saf. 21, 2956–3009. https://doi.org/10.1111/1541-4337.12958.

Dupont, F.M., Altenbach, S.B., 2003. Molecular and biochemical impacts of environmental factors on wheat grain development and protein synthesis. J. Cereal Sci. 38, 133–146. https://doi.org/10.1016/S0733-5210(03)00030-4.

Goriewa-Duba, K., Duba, A., Wachowska, U., Wiwart, M., 2018. An evaluation of the variation in the morphometric parameters of grain of six triticum species with the use of digital image analysis. Agronomy 8. https://doi.org/10.3390/agronomy8120296.

Halcro, K., McNabb, K., Lockinger, A., Socquet-Juglard, D., Bett, K.E., Noble, S.D., 2020. The BELT and phenoSEED platforms: shape and colour phenotyping of seed samples. Plant. Methods 16, 49. https://doi.org/10.1186/s13007-020-00591-8.

Hu, Y., Zhang, Z., 2021. GridFree: a python package of imageanalysis for interactive grain counting and measuring. Plant. Physiol. 186, 2239–2252. https://doi.org/10.1093/plphys/kiab226.

Kartakoullis, A., Caporaso, N., Whitworth, M.B., Fisk, I.D., 2025. Gaussian mixture model clustering allows accurate semantic image segmentation of wheat kernels from near-infrared hyperspectral images. Chemom. Intell. Lab. Syst. 259, 105341. https://doi.org/10.1016/j.chemolab.2025.105341.

Liu, Q., Zhang, Y., Shi, J., Yang, W., Feng, H., Hu, W., 2025. Hyperspectral imaging of grains uncovers the genetic architecture of nitrogen response of development in bread wheat. Mol. Breed. 45, 88. https://doi.org/10.1007/s11032-025-01609-6.

Mahato, G., Graebner, R.C., Hunt, M.P., Namdar, G., Plunkett, R., Wood, D., Krause, M., Singh, S., Calderon, F.J., Hagerty, C., 2026. Comparative analysis of wheat grain protein content: wet chemistry and NIR based methods. Food Anal. Methods 19, 208. https://doi.org/10.1007/s12161-026-03123-7.

Manley, M., McGoverin, C.M., Engelbrecht, P., Geladi, P., 2012. Influence of grain topography on near infrared hyperspectral images. Talanta 89, 223–230. https://doi.org/10.1016/j.talanta.2011.11.086.

Martín-Gómez, J.J., Rewicz, A., Goriewa-Duba, K., Wiwart, M., Tocino, Á., Cervantes, E., 2019. Morphological description and classification of wheat kernels based on geometric models. Agronomy 9. https://doi.org/10.3390/agronomy9070399.

Neuman, M., Sapirstein, H.D., Shwedyk, E., Bushuk, W., 1987. Discrimination of wheat class and variety by digital image analysis of whole grain samples. J. Cereal Sci. 6, 125–132. https://doi.org/10.1016/S0733-5210(87)80049-8.

Osborne, B.G., 1984. Investigations into the use of near infrared reflectance spectroscopy for the quality assessment of wheat with respect to its potential for bread baking. J. Sci. Food Agric. 35, 106–110. https://doi.org/10.1002/jsfa.2740350117.

Osborne, B.G., 1987. Determination of moisture in white flour, ground wheat and whole wheat by near infrared reflectance using a single calibration. J. Sci. Food Agric. 38, 341–346. https://doi.org/10.1002/jsfa.2740380406.

Ramaj, I., Romuli, S., Schock, S., Müller, J., 2024. Discrete element modelling of bulk behaviour of wheat (*Triticum aestivum* L.) cv. 'Pionier' during compressive loading. Biosyst. Eng. 242, 123–139. https://doi.org/10.1016/j.biosystemseng.2024.04.005.

Sadeghi, M., Babaeian, E., Tuller, M., Jones, S.B., 2018. Particle size effects on soil reflectance explained by an analytical radiative transfer model. Remote. Sens. Environ. 210, 375–386. https://doi.org/10.1016/j.rse.2018.03.028.

Schierenbeck, M., Alqudah, A.M., Lohwasser, U., Tarawneh, R.A., Simón, M.R., Börner, A., 2021. Genetic dissection of grain architecture-related traits in a winter wheat population. BMC Plant. Biol. 21, 417. https://doi.org/10.1186/s12870-021-03183-3.

Sharma, R., Kumar, M., Alam, M.S., 2021. Image processing techniques to estimate weight and morphological parameters for selected wheat refractions. Sci. Rep. 11, 20953. https://doi.org/10.1038/s41598-021-00081-4.

Symons, S.J., Fulcher, R.G., 1988. Determination of wheat kernel morphological variation by digital image analysis: I. Variation in Eastern Canadian milling quality wheats. J. Cereal Sci. 8, 211–218. https://doi.org/10.1016/S0733-5210(88)80032-8.

Wang, D., Dowell, F.E., Lacey, R.E., 1999. Single wheat kernel size effects on near-infrared reflectance spectra and color classification. Cereal Chem. 76, 34–37.

Wang, K., Taylor, D., Ruan, Y., Pozniak, C.J., Izydorczyk, M., Fu, B.X., 2023. Unveiling the factors affecting milling quality of durum wheat: influence of kernel physical properties, grain morphology and intrinsic milling behaviours. J. Cereal Sci. 113, 103755. https://doi.org/10.1016/j.jcs.2023.103755.

Williams, P.C., 2020. Application of chemometrics to prediction of some wheat quality factors by near-infrared spectroscopy. Cereal Chem. 97, 958–966. https://doi.org/10.1002/cche.10318.

Yabwalo, D.N., Berzonsky, W.A., Brabec, D., Pearson, T., Glover, K.D., Kleinjan, J.L., 2018. Impact of grain morphology and the genotype by environment interactions on test weight of spring and winter wheat (Triticum aestivum L.). Euphytica 214, 125. https://doi.org/10.1007/s10681-018-2202-7.

Zhang, X., Lin, T., Xu, J., Luo, X., Ying, Y., 2019. DeepSpectra: an end-to-end deep learning approach for quantitative spectral analysis. Anal. Chim. Acta 1058, 48–57. https://doi.org/10.1016/j.aca.2019.01.002.

Zhihong, M., Yuhan, M., Liang, G., Chengliang, L., 2016. Smartphone-Based Visual Measurement and Portable Instrumentation for Crop Seed Phenotyping. IFAC-Pap., 5th IFAC Conference on Sensing, Control and Automation Technologies for Agriculture AGRICONTROL 2016 49, 259–264. https://doi.org/10.1016/j.ifacol.2016.10.048.